

Micromagnetic simulation of high-power spin-torque oscillator in half-metallic Heusler alloy spin valve nanopillar

H. B. Huang, X. Q. Ma, Z. H. Liu, C. P. Zhao, and L. Q. Chen

Citation: *AIP Advances* **3**, 032132 (2013); doi: 10.1063/1.4796189

View online: <http://dx.doi.org/10.1063/1.4796189>

View Table of Contents: <http://aipadvances.aip.org/resource/1/AAIDBI/v3/i3>

Published by the [American Institute of Physics](#).

Additional information on AIP Advances

Journal Homepage: <http://aipadvances.aip.org>

Journal Information: <http://aipadvances.aip.org/about/journal>

Top downloads: http://aipadvances.aip.org/most_downloaded

Information for Authors: <http://aipadvances.aip.org/authors>

ADVERTISEMENT

Explore AIP's open access journal:

- Rapid publication
- Article-level metrics
- Post-publication rating and commenting

Micromagnetic simulation of high-power spin-torque oscillator in half-metallic Heusler alloy spin valve nanopillar

H. B. Huang,^{1,2} X. Q. Ma,^{1,a} Z. H. Liu,¹ C. P. Zhao,¹ and L. Q. Chen²

¹Department of Physics, University of Science and Technology Beijing, Beijing, 100083, China

²Department of Materials Science and Engineering, The Pennsylvania State University, University Park, PA 16802, USA

(Received 2 July 2012; accepted 8 March 2013; published online 15 March 2013)

We investigated the spin-torque oscillator in a half-metallic Heusler alloy Co_2MnSi (CMS) spin-valve nanopillar using micromagnetic simulations. Although it is known that the out-of-plane precession (OPP) usually has a larger power output than the in-plane precession (IPP), only IPP mode was experimentally observed in CMS. Our simulations revealed the fundamental and second harmonic radio frequency (rf) oscillations of the IPP mode, consistent with the experimental measurements in CMS-based pillars. Our simulations predicted that the OPP mode can be obtained under the condition of an initially antiparallel state, a small external magnetic field, and a sufficiently large current density. *Copyright 2013 Author(s). This article is distributed under a Creative Commons Attribution 3.0 Unported License. [http://dx.doi.org/10.1063/1.4796189]*

I. INTRODUCTION

The spin-transfer torque (STT), the transfer of angular momentums from the electrons of the spin-polarized current to the ferromagnet, was initially proposed by Slonczewski¹ and Berger² in 1996. STT can induce uniform precession of the ferromagnetic magnetization about the axis of the effective field. This high-frequency precession has been studied in spin valve multilayers in both nanopillar³⁻⁵ and point contact⁶⁻⁸ geometries. Coupled with the giant magnetoresistance effect (GMR), this precession produces a voltage response that makes these devices high-frequency oscillators, called spin torque nano-oscillators (STNO), opening up the possibilities of new spintronic applications. STNO has various attractive advantages, e.g., high frequency microwave (2 GHz~100 GHz), narrow output band with high Q values > 10 000, tunable over a wide range of frequencies via applied field or current, and voltage outputs in the mV regime. However, increasing output power is a difficult technical challenge that needs to be overcome for any useful application. Many attempts have been made to increase the output power, e.g., an effective way to increase output power is a magnetic tunnel junction (MTJ) based STNO with a larger linewidth.⁹⁻¹² Compared with MTJ-STNO, the advantages of using STNO in a full metal GMR structure are narrow oscillation linewidth and low device resistance enabling good impedance matching. However, the lower output power of the conventional 3d-FM-based GMR structure is the biggest problem for designing applicable STNO device. The output power of STNO is proportional to the square of its magnetoresistance (MR) ratio. If high polarization materials like Heusler alloys are used, it could increase the GMR signal¹³⁻¹⁶ and hence the power output from the oscillator.

Comparing with other alloys used for STNO, Heusler alloys have lower saturation magnetization M_s ,¹⁷ smaller Gilbert damping constant α ,¹⁸ higher spin polarization factor η ¹⁹ and higher GMR ratio.^{20,21} Especially, the full-Heusler alloy Co_2MnSi has attracted strong interest due to a large minority spin band gap of ~ 0.4 eV at the Fermi level²² and the highest Curie temperature (985 K)

^aCorresponding author. Tel.: +86-10-62334074; fax.: +86-10-62327283, E-mail address: xqma@sas.ustb.edu.cn (X. Q. Ma)



among the known half- and full-Heusler alloys.²³ All these advantages are beneficial to reducing the critical current of the magnetization precession and to increasing the output power. Okura *et al.*²⁴ found that a large MR ratio of 12.5% can be obtained in Co₂MnSi (CMS) alloy arising from its large spin polarization, and a high rf output power of 1.1 nW was achieved in spite of a small precession angle of 8.6° of in-plane precession mode (IPP). They predicted that the output power could be significantly enhanced if the precession angle is increased by using the out-of-plane precession (OPP) mode. Sinha *et al.*²⁵ observed large emission amplitudes exceeding 150 nV/Hz and narrow generation linewidth below 10 MHz by setting the external magnetic field magnitude or angle and current to an optimum value. However, there have been no reports on the OPP mode of the Heusler alloy STNO even though its mechanism was well established.^{26–28} We previously studied the unsymmetrical two-step switching in the Heusler alloy Co₂FeAl_{0.5}Si_{0.5} spin valve by using micromagnetic simulations²⁹ and obtained results consistent with experiment.³⁰ In this paper, we investigated the condition for achieving the OPP mode of CMS Heusler alloy in order to enhance the rf output power.

II. THEORETICAL MODEL

We studied a CMS-based spin valve device with the structure of CMS (10 nm)/Ag (4 nm)/CMS (2 nm) and the elliptical cross section area of $64 \times 128 \text{ nm}^2$ (Figure 1). Comparing with the experimental structure, we reduce the thickness of free and pinned layers to get smaller critical current of magnetization precession. We employ a Cartesian coordinate system where the x-axis is the long axis of the ellipse and the y-axis the short axis. The samples were discretized in computational cells of $2 \times 2 \times 2 \text{ nm}^3$. A positive current is defined as a current flowing from the pinned layer to the free layer. The two CMS layers are separated by a thin Ag layer, and the top CMS layer is the free layer whose magnetization dynamics is triggered by a spin-polarized current. The bottom CMS layer is the fixed layer with the initial magnetization \mathbf{P} along the positive x axis. In our simulation, the initial magnetization vector \mathbf{M} of the layer is along the negative x axis. This antiparallel configuration between the pinned layer and the free layer is different from the parallel configuration in the experiment under an external magnetic field of 450 Oe. Different from the experiment in which a positive current was applied, we apply a negative current since our initial state is antiparallel. The external magnetic field in our simulation is increased step by step from zero to 302 Oe in order to obtain all the dynamics of free layer magnetization. We not only obtained results for the IPP mode consistent with experiments but also observed the OPP mode predicted by Okura *et al.*²⁴ The middle Ag layer is a spacer layer whose function is to avoid the exchange coupling between the two CMS layers. The thickness of the spacer layer (4 nm) is much smaller than the spin diffusion length to conserve the spin momentum. In our simulations, we describe the dynamics of \mathbf{M} using a generalized Landau-Lifshitz-Gilbert-Slonczewski (LLGS) equation,¹

$$\begin{aligned} \frac{d\mathbf{M}}{dt} = & -\gamma' \mathbf{M} \times \mathbf{H}_{\text{eff}} - \frac{\alpha \gamma'}{M_s} \mathbf{M} \times (\mathbf{M} \times \mathbf{H}_{\text{eff}}) - \frac{2\mu_B J}{(1 + \alpha^2) e d M_s^3} g(\mathbf{M}, \mathbf{P}) \mathbf{M} \times (\mathbf{M} \times \mathbf{P}) \\ & + \frac{2\mu_B \alpha J}{(1 + \alpha^2) e d M_s^2} g(\mathbf{M}, \mathbf{P}) (\mathbf{M} \times \mathbf{P}) \end{aligned} \quad (1)$$

where \mathbf{H}_{eff} is the effective field, $\gamma' = \gamma/(1 + \alpha^2)$, γ is the electron gyromagnetic ratio, and α is the dimensionless damping parameter. The effective field includes anisotropy, demagnetization, external, and exchange fields, namely, $\mathbf{H}_{\text{eff}} = \mathbf{H}_{\text{ex}} + \mathbf{H}_{\text{anis}} + \mathbf{H}_{\text{dem}} + \mathbf{H}_{\text{ext}}$. The ‘‘Gilbert damping’’ term in Eq. (1) takes into account the energy dissipation mechanisms.

The last two terms on the right side of Eq. (1) describe STT which tends to drag the magnetization away from its initial state and drives the magnetization precession. μ_B , J , d , e , M_s , are the Bohr magneton, the current density, the thickness of the free layer, the electron charge and the saturation magnetization, respectively. Here, we only consider the first term of transverse torque and ignore the second term of smaller field-like torque since the field-like torque is very small in metallic alloys.^{31,32} The scalar function $g(\mathbf{M}, \mathbf{P})$ is given by¹

$$g(\mathbf{M}, \mathbf{P}) = [-4 + (1 + \eta)^3 (3 + \mathbf{M} \cdot \mathbf{P} / M_s^2) / 4\eta^{3/2}]^{-1} \quad (2)$$

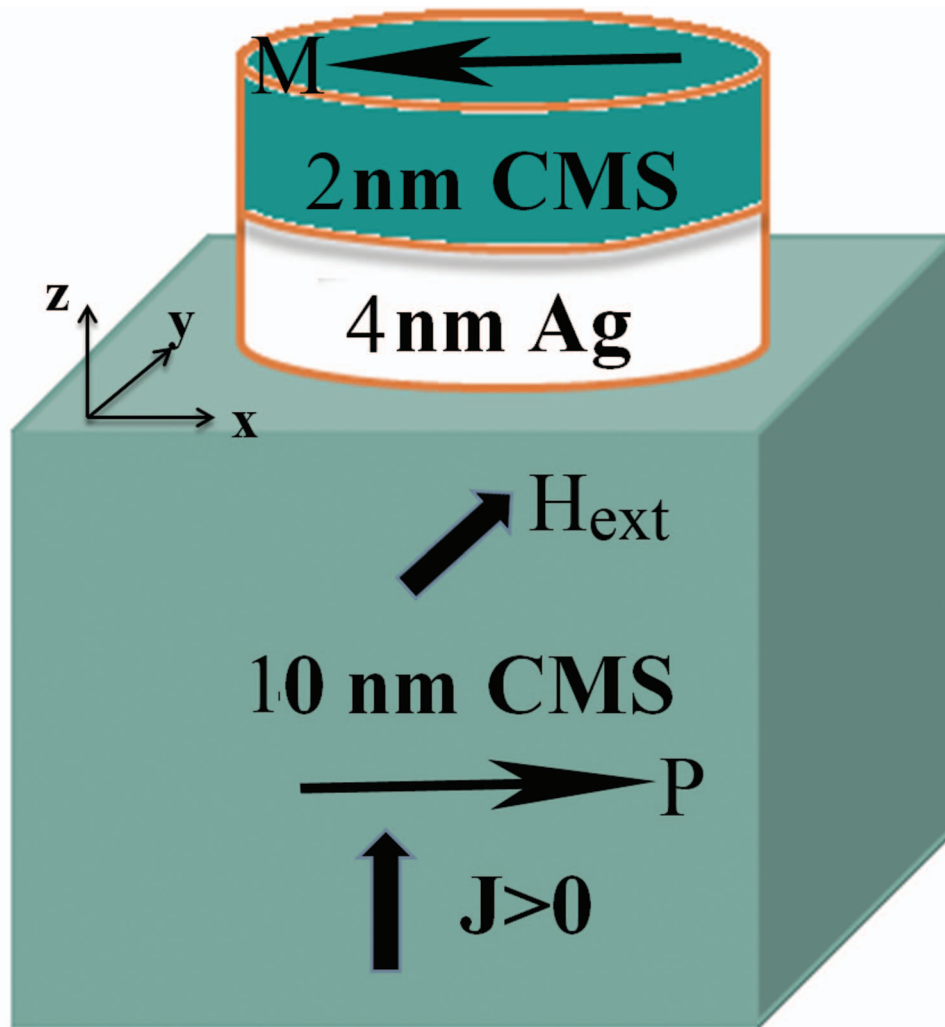


FIG. 1. Schematic illustration of Co_2MnSi (CMS)/Ag/CMS CPP-GMR nanopillar.

where η is the spin polarization factor, the angle between \mathbf{M} and \mathbf{P} is θ . $\mathbf{M} \cdot \mathbf{P}/M_s^2 = \cos \theta$.

The dynamics of magnetization is investigated by numerically solving the time-dependent LLGS equation using finite difference method together with the Gauss-Seidel projection method,³³ with a constant time step $\Delta t = 0.0268858$ ps.^{34,35} We adopted the following magnetic parameters, saturation magnetization $M_s = 8.0 \times 10^5 \text{ A/m}$ ³⁶ smaller than the experimental value for thinner thickness, exchange constant $A = 2.0 \times 10^{-11} \text{ J/m}$,³⁷ and magnetocrystalline anisotropy constant $K_1 = 3.0 \times 10^3 \text{ J/m}^3$.³⁸ Other parameters are Gilbert damping parameter $\alpha = 0.008$,^{38,39} and spin polarization factor $\eta = 0.56$,^{40,41} and electron gyromagnetic ratio $\gamma = 2.3245 \times 10^5 \text{ m/(A} \cdot \text{s)}$. Although half-metallic ferromagnets have been proposed as candidates for spin injection devices because they have been predicted to exhibit 100% spin polarization, most experiments could not reach the perfectly spin-polarized state due to partial chemical disorder in the lattice.⁴² For example, a single crystal of Co_2MnSi grown by the Czochralski method, an Andreev-reflection measurement showed a value of 56% spin polarization.⁴¹ Therefore, in our simulations, we simply assumed 56% spin polarization. We previously studied Co/Cu/Co nanopillar spin valve of non-half-metallic spin-polarization,⁴³ we only observed IPP without an external magnetic field. Using a higher spin polarization constant can decrease the critical current density, but did not lead to the OPP. To verify the validity of our simulation, we first investigated the magnetization dynamics under an external

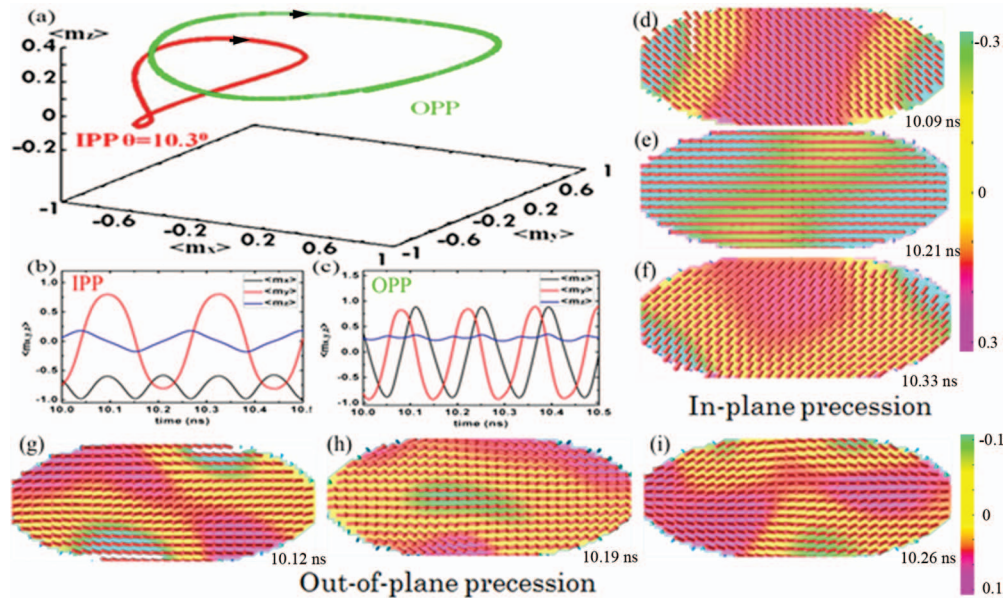


FIG. 2. (a) Magnetization trajectories of in-plane precession (IPP) (red) under the current density of $-1.0 \times 10^6 \text{ A/cm}^2$ and out-of-plane precession (OPP) (green) under the current density of $-8.0 \times 10^6 \text{ A/cm}^2$ (b) IPP temporal evolutions of $\langle m_x \rangle$ (black), $\langle m_y \rangle$ (red) and $\langle m_z \rangle$ (blue) under the current density of $-1.0 \times 10^6 \text{ A/cm}^2$. (c) OPP temporal evolution of $\langle m_x \rangle$ (black), $\langle m_y \rangle$ (red) and $\langle m_z \rangle$ (blue) under the current density of $-8.0 \times 10^6 \text{ A/cm}^2$. (d)~(f) Magnetization distributions of IPP. (g)~(i) Magnetization distributions of OPP.

magnetic field. In our simulations, the magnetization switched from the initial stable state along $-x$ axis to the final stable state along the $+y$ axis when the external magnetic field of 403 Oe is applied in the short axis of the ellipsoidal pillar along y axis direction, which is consistent with the experiment result in Figure 1(b) of Ref. 24.

III. RESULTS AND DISCUSSION

Figure 2(a) shows the magnetization trajectories of IPP and OPP under an external field of 50 Oe along the y -axis with current densities of $-1.0 \times 10^6 \text{ A/cm}^2$ and $-8.0 \times 10^6 \text{ A/cm}^2$, respectively. We obtained the magnetization precession angle of 10.3° in IPP mode, which is very close to 8.6° from the experiment. Based on Figure 2(b), there is no significant change in the magnitude of $\langle m_x \rangle$ during precession, but $\langle m_y \rangle$ varies over a wide range, and $\langle m_z \rangle$ changes its sign. The $\langle m_x \rangle$ component oscillates twice during one complete precession cycle, and hence its oscillation frequency is approximately twice those of $\langle m_y \rangle$ and $\langle m_z \rangle$. As the current density increases, the magnetization evolution changes to the out-of-plane precession mode. In this mode, the magnetization rotates on the x - y plane with the magnetization precession angle of 73.1° , but $\langle m_z \rangle$ does not change its sign and varies little as shown in Figure 2(c). Similarly, $\langle m_z \rangle$ has two oscillations when the components of $\langle m_x \rangle$ and $\langle m_y \rangle$ endure one. The spatial magnetization distributions during IPP and OPP are shown in Figures 2(d)–2(f) and 2(g)–2(i). The six snapshots of magnetization distributions correspond to the temporal evolution of magnetization in Figures 2(b) and 2(c). The colors represent the magnitude of the magnetization components $\langle m_z \rangle$ ($-0.3 \sim 0.3$) for IPP mode and ($-0.1 \sim 0.1$) for OPP mode while the arrows indicate the magnetization projection on the plane Oxy , through which the magnetization components $\langle m_x \rangle$ and $\langle m_y \rangle$ were shown. It can be seen that the domain, characterized as a uniform precession of the arrows in IPP mode, rotates clockwise on the x - y plane. The uniform precession results from the small applied current density. For the spatial magnetization component $\langle m_z \rangle$, the oscillations are initially excited at the edges of the free layer because of spatially non-uniform local demagnetization fields⁴⁴ and then spread out to the center of free layer. The domain arrows for OPP mode also rotates clockwise, and the arrows precess periodically from the $-x$ direction to the

+x direction. In contrast to IPP, a non-uniform precession of the domain arrows was found in the evolution of OPP domain configuration. We can attribute this non-uniform precession to the high current density. The non-uniform precession increases the linewidth. The high current density can result to the increase of the linewidth and the output power. To get the narrow linewidth and maintain the high output power, we need to find what factors play a dominant role in determining the field magnitude at which the linewidth takes its minimum. From our simulation results, the appropriate value of magnetic field 50 Oe and current density $-8.6 \times 10^6 \text{ A/cm}^2$ will suppress the non-uniform precession and lead to the narrow linewidth while maintaining high output power. Furthermore, the reason for using the initial antiparallel structure could be elucidated by Slonczewski's model¹ of the Eq. (2), which takes into account the interface spin-flip scattering between the layers. In this model, the relationship of STT versus θ is not symmetrical about 90° using the STT reaches its maximum value at the angle about 162° as shown in the figure 2(b) of Ref. 29. The spin transfer torque from 180° to 0° will increase faster than STT from 0° to 180° . Therefore, the generation of the magnetization precession of antiparallel structure is easier than parallel structure due to different magnitude of STT.²⁹

Figure 3(a) shows the power spectral density (PSD) of IPP mode with the increase of current densities under the constant external magnetic field of $H_{\text{ext}} = 302 \text{ Oe}$ along the short axis of the ellipsoidal pillar. For clarity, all the spectra are shifted vertically. As the current density increases to $-7.0 \times 10^5 \text{ A/cm}^2$, two peaks appeared at 3.7 GHz and 7.4 GHz. The higher peak frequencies were twice as high as the lower peak frequencies. The lower frequencies peaks were the fundamental peaks (f_0) and the higher ones were the second harmonics ($2f_0$). This is due to the fact that $\langle m_x \rangle$ oscillates twice during one complete precession cycle, and the oscillation frequency of $\langle m_x \rangle$ is approximately twice those of $\langle m_y \rangle$ and $\langle m_z \rangle$ components. Therefore, the magnetization oscillation gives rise to a resistance oscillation at twice f_0 in the experiment.⁴⁵ In general, the fundamental mode has the highest power than the second harmonics. However, the output power of the second harmonics is larger than the fundamental mode in our simulation of Heusler-based spin valve nanopillar. This phenomenon resulted from the suppression of the large external magnetic field. We performed a test simulation of IPP at a smaller external magnetic field of 80 Oe, the results indicated that the output power of fundamental mode was larger than the second harmonics. For example, the fundamental power of IPP is 0.35, which is larger than the second harmonics power of 0.12. Comparing with the experiment, the magnitude of fundamental peaks is smaller. We attribute to smaller drive current $\sim 10^5 \text{ A/cm}^2$ than the experiment of 10^7 A/cm^2 due to thinner CMS-based free layer in our simulation. The peak frequencies as a function of current are summarized in the right insets. f_0 and $2f_0$ did not vary significantly with current, indicating that the nonlinearity of rf oscillation was suppressed by applying H_{ext} in the short axis. In our simulation, we explain the suppression by the inset which shows that the trajectories do not change with the increase of current. However, the left insets showed that with the increase of current, the frequency of precession decreases (red shift), and the trajectories of IPP broaden from the red trajectory to the blue trajectory under zero magnetic field. Figure 3(b) shows PSD of OPP under $H_{\text{ext}} = 50 \text{ Oe}$ at different current densities. Only one peak frequency was found in this mode since $\langle m_x \rangle$ has one oscillation within a period. The peak frequencies do not change remarkably as the current density increases since the trajectories do not change with the current. However the peak intensities increase with the increase of current densities from $-8.0 \times 10^6 \text{ A/cm}^2$ to $-8.6 \times 10^6 \text{ A/cm}^2$. From the value of P_{out} for the fundamental peak ($P_{\text{out}}^{\text{Fund}}$), the precession angle ($\Delta\theta$) of rf oscillation was roughly estimated by using⁹ $P_{\text{out}}^{\text{Fund}}/P_{\text{in}} \approx \{[(R_{\text{AP}}-R_{\text{P}})R(\theta_0)/R_{\text{AP}}R_{\text{P}}]^2(\Delta\theta/2)^2 \sin^2\theta_0\}/8$, where P_{in} is the input power, and R_{AP} , R_{P} are the device resistance in the antiparallel and parallel states, respectively. P_{out} for the fundamental peak is proportional to $P_{\text{out}} \sim R(\theta)I^2(\Delta\theta/2)^2 \sin^2\theta$, and $\Delta\theta_{\text{IPP}}$ and $\Delta\theta_{\text{OPP}}$ are given by the maximum excursions of the free layer magnetization during the precessional motion on IPP or OPP trajectories. Based on the experimental data of the maximum $\Delta R \sim 0.95 \Omega$ and using the angles of 10.3° in IPP mode and 73.1° in OPP mode, respectively The R_{IPP} and R_{OPP} are determined to be 7.858Ω and 8.172Ω . $(\Delta\theta_{\text{IPP}}/2)^2$ and $(\Delta\theta_{\text{OPP}}/2)^2$ are 26.5 and 1335.9. Based on the magnitude of current density, we can conclude that $P_{\text{out}}^{\text{OPP}}/P_{\text{out}}^{\text{IPP}} \sim 5000$. Furthermore, for the IPP case, the magnitude of power output would be 0.35 when a small external magnetic field of 80 Oe and a current density of $9.0 \times 10^5 \text{ A/cm}^2$ were applied. The output power 0.35 at 80 Oe is larger than the power of 0.01 at

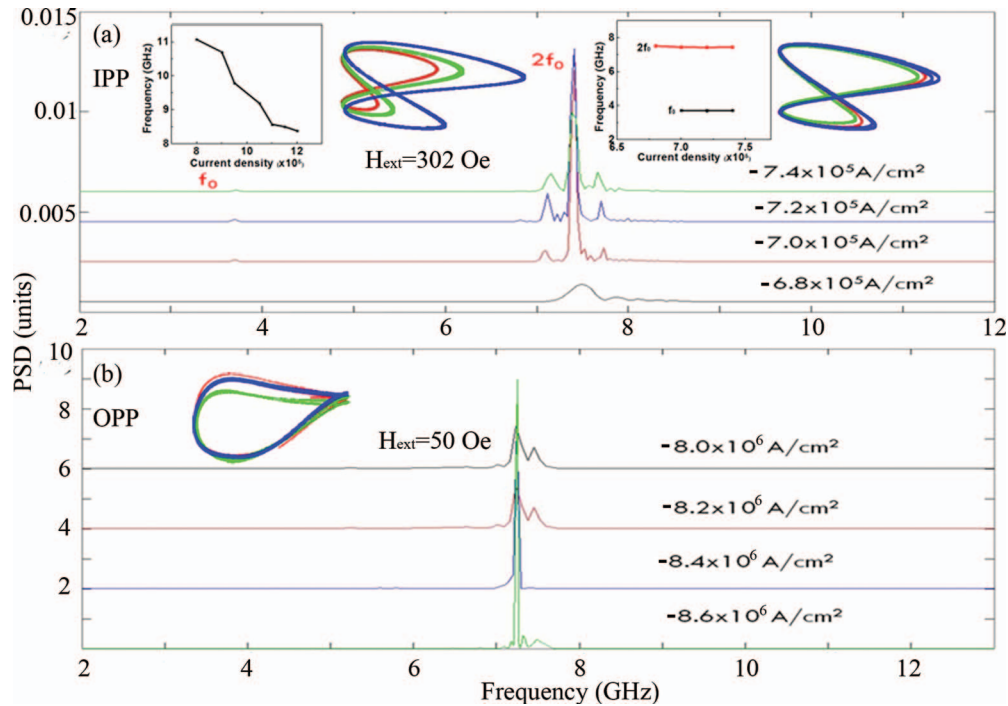


FIG. 3. (a) PSD of IPP as the increase of current densities under the constant external magnetic field of $H_{\text{ext}} = 302 \text{ Oe}$. Left insets show peak frequency as function of current density and trajectories under zero external magnetic fields. Right insets show peak frequency as function of current density and trajectories under the external magnetic field of 302 Oe. (b) PSD of OPP under $H_{\text{ext}} = 50 \text{ Oe}$ at different current densities. Inset shows the trajectories of OPP under the external magnetic field of 50 Oe. For clarity, spectra are shifted vertically with different constants.

302 Oe. Therefore the external magnetic field can lead to 35 times increase in output power. Comparing to figures (a) and (b), we found that the maximum output power of OPP is the square of current density times that of IPP, and it can be significantly enhanced to about 2000 ~ 10000 times using OPP mode by increasing the drive current compared with the IPP mode. Therefore, the output power depends on the current, the magnetic field, and the precessional angle. All of them make different contributions to the increase of output power. We conclude that using the out-of-plane precession mode could significantly enhance the output power in the CMS-based STO due to the large MR effect and the large drive current.

IV. CONCLUSIONS

In summary, we investigated the spin-torque oscillator in a half-metallic Heusler alloy Co_2MnSi (CMS) spin-valve nanopillar using micromagnetic simulations. Different characteristics were observed from the snapshots of magnetization distributions between IPP and OPP modes. Fundamental and second harmonic rf oscillations of IPP were clearly observed. Based on the magnetization trajectories at increasing current densities, we demonstrated that the two peak frequencies do not vary significantly with current density under an external magnetic field while they decrease with current density without an applied magnetic field, indicating suppression of the nonlinearity of rf oscillation by an external magnetic field. We obtained the out-of-plane precession mode under the condition of an initial antiparallel state, a small external magnetic field, and a large current. It can be significantly enhanced to about 2000 ~ 10000 times using OPP mode by increasing the drive current compared with the IPP mode.

ACKNOWLEDGMENTS

This work was sponsored by the National Science Foundation of China (11174030), by the US National Science Foundation under the grant number DMR-1006541 (Chen) and in part by the China Scholarship Council. The computer simulations were carried out on the LION and Cyberstar clusters at the Pennsylvania State University.

- ¹J. C. Slonczewski, *J. Magn. Magn. Mater.* **159**, L1 (1996).
- ²L. Berger, *Phys. Rev. B* **54**, 9359 (1996).
- ³J. Z. Sun, D. J. Monsma, M. J. Rooks, and R. H. Koch, *Appl. Phys. Lett.* **81**, 2202 (2002).
- ⁴S. I. Kiselev, J. C. Sankey, I. N. Krivorotov, N. C. Emley, R. J. Schoelkopf, R. A. Buhrman, and D. C. Ralph, *Nature* **425**, 380 (2003).
- ⁵S. Urazhdin, N. O. Birge, W. P. Pratt, and J. Bass, *Phys. Rev. Lett.* **91**, 146803 (2003).
- ⁶M. Tsoi, A. G. M. Jansen, J. Bass, W.-C. Chiang, V. Tsoi, and P. Wyder, *Nature* **406**, 46 (2000).
- ⁷W. H. Rippard, M. R. Pufall, S. Kaka, S. E. Russek, and T. J. Silva, *Phys. Rev. Lett.* **92**, 027201 (2004).
- ⁸T. Y. Chen, Y. Ji, C. L. Chien, and M. D. Stiles, *Phys. Rev. Lett.* **93**, 026601 (2004).
- ⁹A. M. Deac, A. Fukushima, H. Kubota, H. Maehara, Y. Suzuki, S. Yuasa, Y. Nagamine, K. Tsunekawa, D. D. Djayaprawira, and N. Watanabe, *Nat. Phys.* **4**, 803 (2008).
- ¹⁰D. Houssameddine, S. H. Florez, J. A. Katine, J. P. Michel, U. Ebels, D. Mauri, O. Ozatay, B. Delaet, B. Viala, L. Folks, B. D. Terris, and M. C. Cyrille, *Appl. Phys. Lett.* **93**, 022505 (2008).
- ¹¹Z. M. Zeng, P. Upadhyaya, P. K. Amiri, K. H. Cheung, J. A. Katine, J. Langer, K. L. Wang, and H. W. Jiang, *Appl. Phys. Lett.* **99**, 032503 (2011).
- ¹²K. Mizushima, T. Nagasawa, K. Kudo, Y. Saito, and R. Sato, *Appl. Phys. Lett.* **94**, 152501 (2009).
- ¹³T. Marukame, T. Ishikawa, S. Hakamata, K. Matsuda, T. Uemura, and M. Yamamoto, *Appl. Phys. Lett.* **90**, 012508 (2007).
- ¹⁴H. Wang, A. Sato, K. Saito, S. Mitani, K. Takanashi, and K. Yakushiji, *Appl. Phys. Lett.* **90**, 142510 (2007).
- ¹⁵T. Furubayashi, K. Kodama, H. Sukegawa, Y. K. Takahashi, K. Inomata, and K. Hono, *Appl. Phys. Lett.* **93**, 122507 (2008).
- ¹⁶N. Tezuka, N. Ikeda, S. Sugimoto, and K. Inomata, *Appl. Phys. Lett.* **89**, 252508 (2006).
- ¹⁷O. Gaier, J. Hamrle, S. J. Hermsdoerfer, H. Schultheiß, B. Hillebrands, Y. Sakuraba, M. Oogane, and Y. Ando, *J. Appl. Phys.* **103**, 103910 (2008).
- ¹⁸R. Yilgin, M. Oogane, Y. Ando, and T. Miyazaki, *J. Magn. Magn. Mater.* **310**, 2322 (2007).
- ¹⁹R. Shan, H. Sukegawa, W. Wang, M. Kodzuka, T. Furubayashi, T. Ohkubo, S. Mitani, K. Inomata, and K. Hono, *Phys. Rev. Lett.* **102**, 246601 (2009).
- ²⁰W. Wang, H. Sukegawa, R. Shan, S. Mitani, and K. Inomata, *Appl. Phys. Lett.* **95**, 182502 (2009).
- ²¹K. Yakushiji, K. Saito, S. Mitani, K. Takanashi, Y. K. Takahashi, and K. Hono, *Appl. Phys. Lett.* **88**, 222504 (2006).
- ²²S. Fujii, S. Sugimura, S. Ishida, and S. Asano, *J. Phys.: Condens. Matter* **2**, 8583 (1990).
- ²³P. J. Brown, K. U. Neumann, P. J. Webster, and K. R. A. Ziebeck, *J. Phys.: Condens. Matter* **12**, 1827 (2000).
- ²⁴R. Okura, Y. Sakuraba, T. Seki, K. Izumi, M. Mizuguchi, and K. Takanashi, *Appl. Phys. Lett.* **99**, 052510 (2011).
- ²⁵J. Sinha, M. Hayashi, Y. K. Takahashi, T. Taniguchi, M. Drapeko, S. Mitani, and K. Hono, *Appl. Phys. Lett.* **99**, 162508 (2011).
- ²⁶Y. Zhou, J. Persson, S. Bonetti, and J. Åkerman, *Appl. Phys. Lett.* **92**, 092505 (2008).
- ²⁷O. Boulle, V. Cros, J. Grollier, L. G. Pereira, C. Deranlot, and F. Petroff, *Phys. Rev. B* **77**, 174403 (2008).
- ²⁸E. Jaromirska, P. Baláz, L. López Díaz, and J. Barnaś, *Phys. Rev. B* **81**, 014408 (2010).
- ²⁹H. B. Huang, X. Q. Ma, Z. H. Liu, F. Y. Meng, Z. H. Xiao, P. P. Wu, S. Q. Shi, and L. Q. Chen, *J. Appl. Phys.* **110**, 033913 (2011).
- ³⁰H. Sukegawa, S. Kasai, T. Furubayashi, S. Mitani, and K. Inomata, *Appl. Phys. Lett.* **96**, 042508 (2010).
- ³¹M. A. Zimmler, B. Özyilmaz, W. Chen, A. D. Kent, J. Z. Sun, M. J. Rooks, and R. H. Koch, *Phys. Rev. B* **70**, 184438 (2004).
- ³²H. Meng and J. P. Wang, *Appl. Phys. Lett.* **88**, 172506 (2006).
- ³³X. P. Wang, C. J. García-Cervera, and E. Weinan, *J. Comput. Phys.* **171**, 357 (2001).
- ³⁴J. X. Zhang, and L. Q. Chen, *Acta Mater.* **53**, 2845 (2005).
- ³⁵Z. H. Xiao, X. Q. Ma, P. P. Wu, J. X. Zhang, L. Q. Chen, and S. Q. Shi, *J. Appl. Phys.* **102**, 093907 (2007).
- ³⁶B. Balke, G. H. Fecher, H. C. Kandpal, C. Felser, K. Kobayashi, E. Ikenaga, J. J. Kim, and S. Ueda, *Phys. Rev. B* **74**, 104405 (2006).
- ³⁷J. Hamrle, O. Gaier, S. G. Min, B. Hillebrands, Y. Sakuraba, and Y. Ando, *J. Appl. Phys.* **42**, 084005 (2009).
- ³⁸R. Yilgin, Y. Sakuraba, M. Oogane, S. Mizumaki, Y. Ando, and T. Miyazaki, *Japan. J. Appl. Phys.* **46**, L205 (2007).
- ³⁹R. Yilgin, M. Oogane, Y. Ando, and T. Miyazaki, *J. Magn. Magn. Mater.* **310**, 2322 (2007).
- ⁴⁰S. Picozzi, A. Continenza, and A. J. Freeman, *Phys. Rev. B* **66**, 094421 (2002).
- ⁴¹L. Ritchie, G. Xiao, Y. Ji, T. Y. Chen, C. L. Chien, M. Zhang, J. L. Chen, Z. H. Liu, G. H. Wu, and X. X. Zhang, *Phys. Rev. B* **68**, 104430 (2003).
- ⁴²W. H. Wang, M. Przybylski, W. Kuch, L. I. Chelaru, J. Wang, Y. F. Lu, J. Barthel, and J. Kirschner, *J. Magn. Magn. Mater.* **286**, 336 (2005).
- ⁴³X. Q. Ma, Z. H. Xiao, P. P. Wu, J. X. Zhang, S. Q. Shi and L. Q. Chen, *J. Appl. Phys.* **103**, 07B111 (2008).
- ⁴⁴K. J. Lee, A. Deac, O. Redon, J. P. Nozières, and B. Dieny, *Nat. Mater.* **1237**, 877 (2004).
- ⁴⁵D. Berkov and N. Gorn, *Phys. Rev. B* **71**, 052403 (2005).